Phase-field lattice Boltzmann model for interface tracking of a binary fluid system based on the Allen-Cahn equation

Y. Q. Zu,[*] A. D. Li, and H. Wei

Department of Aeronautics and Astronautics, Fudan University, 220 Handan Road, Shanghai, 200433, China

A lattice Boltzmann (LB) model is proposed to track the interface of binary fluid system based on the conservative-form Allen-Cahn (A-C) equation for phase field. Utilizing an equilibrium distribution function and a modified LB equation, this model is able to correctly recover the conservative A-C equation through the Chapman-Enskog analysis. A series of two-dimensional (2D) and three-dimensional (3D) phase-capturing benchmark tests have been conducted for validation, which include the diagonal translation of a circular interface, the rigid-body rotation of a Zalesak disk, and the deformation of 2D circular interface and 3D spherical interface in shear flows, all illustrating better accuracy and stability of the proposed model than the previous models tested. By coupling the incompressible hydrodynamic equation, a stationary droplet, a spinodal decomposition, and the Rayleigh-Taylor instability are simulated as well, showing the satisfying performance of the model in dealing with complex interfaces of binary fluid systems.

I. INTRODUCTION

Binary fluid flows are universal in both nature and engineering applications. Major challenges in modeling such flows include dealing with phase segregation and interface dynamics. Thus, it is desirable to develop efficient and accurate methods for interface tracking. The common approaches used to capture the interface can be classified into two categories: sharp interface methods [1–3] and diffuse interface methods [4–8]. In the sharp interface methods, the binary fluid is separated by the sharp interfaces, and the physical quantities, including density, viscosity, and pressure, are discontinuous. In the diffuse interface methods, the sharp interfaces are replaced by the transitional layers with finite thickness, across which fluid properties are continuous, so that this type of method has great advantage in dealing with binary fluid systems with the extremely complicated topological variation of the interfaces [9].

The phase-field method, as a typical diffuse interface approach, has been of particular attention in recent years and widely used in conventional Computational Fluid Dynamics (CFD) solver [5,6] and lattice Boltzmann (LB) method [10–14] to model complicated interfacial dynamics. In the method, a continuous phase-field variable or so-called order parameter governed by the advection–diffusion-type equation is introduced to identify the different phases and calculate certain properties at the interface such as gradients and curvature, which might be required to model surface tension or other interfacial properties. And, the thermodynamic behavior of the binary fluid system is described by a free-energy functional of the order parameter. Generally, there are two forms of governing equations for the order parameter, i.e.,

Cahn-Hilliard (C-H) equation [15,16] and Allen-Cahn (A-C) equation [17,18]. The C-H equation introduces the chemical potential in the diffusion term. Thus, its diffusion term includes a spatial derivative of fourth order which, numerically, may lead to a reduction in the locality and the accuracy [19,20]. As an alternative, the original Allen-Cahn equation cannot conserve the mass. The conservative A-C equation was first proposed by Sun and Beckemann [17] and then improved by Chiu and Lin [18]. As compared to the C-H equation, the conservative A-C equation is much easier to solve, especially in which only a second-order algorithm is required for the discretization of the diffusion term.

The LB method is a class of mesoscopic approaches that has been developed into an effective numerical scheme for simulating multiphase flows [21–25]. As compared to the conventional CFD [5,6], it has demonstrated numerous computational advantages, including high parallelization efficiency and simple boundary treatment [26–37]. In the past years, some LB models have been proposed for solving C-H equation and A-C equation. Zheng *et al.* [8,38] first proposed an LB model that can exactly recover the C-H equation [5,15,16,39–41]. Later on, Zu and He [42] reported a new LB model that not only recovered the correct C-H equation but also showed evident improvement in terms of accuracy and stability. Liang *et al.* [12,43,44] also recovered the correct C-H equation by introducing a time-derivative term in the source term of the LB equation. It was found that, utilizing multiple-relaxation-time version of LB model, the stability and accuracy in the interface capturing can be further improved [12,44]. In the study of Hu *et al.* [45], the LB model was developed to solve the modified C-H equation in which a source term with two Lagrange multipliers was introduced. The numerical results showed that, for incompressible binary fluids, the method can preserve the total mass and the volume of each component at the same time. To solve the

---

[*]Corresponding author: yzu@fudan.edu.cn

conservative A-C equation, Geier *et al.* [46,47] first proposed an LB algorithm, and showed better accuracy and higher convergence rate over the C-H equation. Then, they further presented a simple LB model for the A-C equation in three dimensions. However, as commented by Ren *et al.* [48], the model of Geier *et al.* [46,47] generated some artificial terms in the recovered interfacial equation. In order to avoid the additional terms, Ren *et al.* [48], Wang *et al.* [9], and Liang *et al.* [49] independently developed three kinds of improved Allen-Cahn-based LB models on the basis of the similar idea, i.e., introducing a time-derivative term in the source term of the LB equation. Moreover, Geier *et al.* [46], Wang *et al.* [9], and Liang *et al.* [49] independently offered an alternative algorithm to calculate the gradient of the order parameter locally but meanwhile brought accuracy losses. In our opinion, calculating the gradient of the order parameter locally, so far, cannot really improve the efficiency of the MPI parallel computing for binary fluid systems, because message passing for the order parameter between the neighboring nodes of distributed-memory computer is not avoidable for the existing diffuse-interface models including phase-field LB models. For an example, Laplacian of the order parameter or equivalent forms always exists in surface tension force terms in the existing diffuse-interface models [14,45,48,50–52], leading to the necessity of such massage passing for the order parameter. Recently, Begmohammadi *et al.* [53] conducted a comparative investigation into the differences between the model proposed by Geier *et al.* [46] and those by Ren *et al.* [48] and Wang *et al.* [9], and found that the additional terms caused by the model of Geier *et al.* [46] are actually negligible under certain conditions so that the accuracy of interface tracking is roughly similar for the different models. Moreover, they derived and presented axisymmetric formulations for the model of Geier *et al.* [46].

In the present work, we propose an LB model that can exactly recover the A-C equation through the Chapman-Enskog analysis. To solve velocity field, we utilize the velocity-based incompressible hydrodynamic equation by Zu and He [42]. The accuracy and stability of the present model will be evaluated and, meanwhile, compared with the previous LB models by simulating a series of benchmark problems.

II. PHASE-FIELD BASED LB MODEL FOR INTERFACE TRACKING

A. Governing equation: Conservative A-C equation

In the phase-field theory for the binary fluid system, an order parameter ϕ is used as the indicator of different fluids, and the thermodynamic behavior of the system can be described by a Landau free-energy function [54] as

$$F = \int_\Omega [\psi(\nabla\phi) + k|\nabla\phi|^2/2]d\Omega, \tag{1}$$

where $\psi(\phi)$ is the bulk free-energy density, k is a positive coefficient, $k|\nabla\phi|^2/2$ denotes the surface energy, and Ω represents the fluid domain of the system. For an isothermal system, $\psi(\phi)$ can be written as [5,40]

$$\psi(\phi) = \beta(\phi - \phi_A)^2(\phi - \phi_B)^2, \tag{2}$$

where the coefficient β is related to the surface tension force and the interfacial thickness; ϕ_A and ϕ_B are the values of ϕ in the bulk of fluids A and B respectively [5,40,41,55].

The variation of the free energy leads to a chemical potential [5,40],

$$\mu_\phi = \frac{\delta F}{\delta \phi} = 4\beta(\phi - \phi_A)(\phi - \phi_B)[\phi - (\phi_A + \phi_B)/2] - k\nabla^2\phi. \tag{3}$$

Then, the equilibrium interface profile can be obtained by minimizing the free energy with respect to the variations in ϕ, i.e., solving $\mu_\phi = 0$. For the one-dimensional plane interface, $\mu_\phi = 0$ allows an interface solution of the following form [56]:

$$\phi(\zeta) = \frac{\phi_A + \phi_B}{2} + \frac{\phi_A - \phi_B}{2}\tanh\left(\frac{2\zeta}{W}\right), \tag{4}$$

where ζ is the coordinate along the interface normal **n**, and W is the interface thickness given by [5,40]

$$W = \frac{4}{|\phi_A - \phi_B|}\sqrt{\frac{k}{2\beta}}. \tag{5}$$

The fluid-fluid surface tension σ is given as [39]

$$\sigma = \frac{|\phi_A - \phi_B|^3}{6}\sqrt{2k\beta}. \tag{6}$$

In the time-dependent situations, the evolution of ϕ can be related to the phase flux density **J** as [46]

$$\frac{\partial \phi}{\partial t} = -\nabla \cdot \mathbf{J}, \tag{7}$$

where t is the time. The flux density **J** is the sum of the convective flux density $\mathbf{J}_C$, the diffusive flux density $\mathbf{J}_D$, and the phase-separation flux density $\mathbf{J}_S$, i.e.,

$$\mathbf{J} = \mathbf{J}_C + \mathbf{J}_D + \mathbf{J}_S, \tag{8a}$$

$$\mathbf{J}_C = \phi\,\mathbf{u}, \tag{8b}$$

$$\mathbf{J}_D = -M\nabla\phi, \tag{8c}$$

where **u** is the velocity and M is a constant diffusion parameter named mobility. The phase-separation flux density $\mathbf{J}_S$ is a function to suppress the diffusion of ϕ so that a predefined interface profile can be reached at the equilibrium state. In order to achieve the equilibrium profile $\phi(\zeta)$ given in Eq. (4), $\mathbf{J}_S$ must be used to cancel out the diffusion of $\phi(\zeta)$, i.e., $\mathbf{J}_S = -\mathbf{J}_D[\phi(\zeta)]$. Thus,

$$\mathbf{J}_S = M\nabla\phi(\zeta). \tag{9}$$

Substituting Eq. (4) into Eq. (9) yields

$$\mathbf{J}_S = M\frac{\partial \phi(\zeta)}{\partial \zeta}\mathbf{n} = \frac{M(\phi_A - \phi_B)}{W}\left[1 - \tanh^2\left(\frac{2\zeta}{W}\right)\right]\mathbf{n}, \tag{10}$$

where the unit normal vector **n** can be calculated by

$$\mathbf{n} = \frac{\nabla\phi}{|\nabla\phi|}. \tag{11}$$

Using Eq. (4), Eq. (10) can be reformulated to be a function of ϕ as

$$\mathbf{J}_S = \mathbf{J}_S(\phi) = \frac{4M(\phi_A - \phi)(\phi - \phi_B)}{W(\phi_A - \phi_B)}\frac{\nabla\phi}{|\nabla\phi|}. \tag{12}$$

Substituting Eqs. (8) and (12) into Eq. (7), the following conservative form A-C equation for phase field can be obtained [18,46,57]:

$$\frac{\partial \phi}{\partial t} + \nabla \cdot (\phi \mathbf{u}) = \nabla \cdot [M(\nabla \phi - \Theta \mathbf{n})], \quad (13)$$

where

$$\Theta = \frac{4(\phi_A - \phi)(\phi - \phi_B)}{W(\phi_A - \phi_B)}. \quad (14)$$

B. LB model for interface tracking

In the present study, the following form of LB equation is proposed to recover the conservative form A-C equation:

$$f_i(\mathbf{x} + \mathbf{c}_i \delta t, t + \delta t) - f_i(\mathbf{x}, t)$$
$$= -\frac{f_i(\mathbf{x}, t) - f_i^{eq}(\mathbf{x}, t)}{\tau} + \lambda [f_i^{eq}(\mathbf{x} + \mathbf{c}_i \delta t, t) - f_i^{eq}(\mathbf{x}, t)], \quad (15)$$

where $\mathbf{x}$ denotes the space coordinate; $f_i(\mathbf{x}, t)$ is the phase-field distribution function (along the ith direction) with the local equilibrium state $f_i^{eq}(\mathbf{x}, t)$; $\mathbf{c}_i$ is the mesoscopic velocity

set; δt is the time step; τ is the relaxation time; and λ is a constant given by

$$\lambda = 2\tau - 1 \quad (16)$$

In order to recover Eq. (13), we define the equilibrium distribution function f_i^{eq} as

$$f_i^{eq} = \begin{cases} \phi - \frac{(1-\omega_0)\Gamma\phi}{(1-\lambda)c_s^2}, & i = 0 \\[2ex] \omega_i \frac{\Gamma\phi + \mathbf{c}_i \cdot (\phi\mathbf{u} + M\Theta\mathbf{n})}{(1-\lambda)c_s^2}, & i \neq 0 \end{cases} \quad (17)$$

where, c_s is the lattice speed of sound; M is the mobility coefficient given by

$$M = (\tau - 1/2)\Gamma \delta t. \quad (18)$$

The parameter Γ can be used to control the mobility coefficient.

Since f_i^{eq} is only a linear function of velocity $\mathbf{u}$, the simple D2Q5 and D3Q7 lattice models can be used for two-dimensional (2D) and three-dimensional (3D) problems. In the commonly used lattice models, the mesoscopic velocity set $\mathbf{c}_i$, the weight factor ω_i, and the speed of sound c_s can be given by the following forms.

D2D5:

$$[\mathbf{c}_0, \mathbf{c}_1, \mathbf{c}_2, \mathbf{c}_3, \mathbf{c}_4]$$
$$= \begin{bmatrix} 0 & 1 & 0 & -1 & 0 \\ 0 & 0 & 1 & 0 & -1 \end{bmatrix} c$$
$$\omega_i = \begin{cases} 1/3, & i = 0 \\ 1/6, & i = 1, ..., 4 \end{cases}, \quad c_s = c/\sqrt{3} \quad (19a)$$

D2Q9:

$$[\mathbf{c}_0, \mathbf{c}_1, \mathbf{c}_2, \mathbf{c}_3, \mathbf{c}_4, \mathbf{c}_5, \mathbf{c}_6, \mathbf{c}_7, \mathbf{c}_8]$$
$$= \begin{bmatrix} 0 & 1 & 0 & -1 & 0 & 1 & -1 & -1 & 1 \\ 0 & 0 & 1 & 0 & -1 & 1 & 1 & -1 & -1 \end{bmatrix} c$$
$$\omega_i = \begin{cases} 4/9, & i = 0 \\ 1/9, & i = 1, ..., 4, \\ 1/36, & i = 5, ..., 8 \end{cases} \quad c_s = c/\sqrt{3} \quad (19b)$$

D3D7:

$$[\mathbf{c}_0, \mathbf{c}_1, \mathbf{c}_2, \mathbf{c}_3, \mathbf{c}_4, \mathbf{c}_5, \mathbf{c}_6]$$
$$= \begin{bmatrix} 0 & 1 & 0 & 0 & -1 & 0 & 0 \\ 0 & 0 & 1 & 0 & 0 & -1 & 0 \\ 0 & 0 & 0 & 1 & 0 & 0 & -1 \end{bmatrix} c$$
$$\omega_i = \begin{cases} 1/8, & i = 0 \\ 1/4, & i = 1, ..., 6 \end{cases}, \quad c_s = c/2. \quad (19c)$$

D3Q15:

$$[\mathbf{c}_0, \mathbf{c}_1, \mathbf{c}_2, \mathbf{c}_3, \mathbf{c}_4, \mathbf{c}_5, \mathbf{c}_6, \mathbf{c}_7, \mathbf{c}_8, \mathbf{c}_9, \mathbf{c}_{10}, \mathbf{c}_{11}, \mathbf{c}_{12}, \mathbf{c}_{13}, \mathbf{c}_{14}]$$
$$= \begin{bmatrix} 0 & 1 & 0 & 0 & -1 & 0 & 0 & 1 & -1 & 1 & 1 & -1 & 1 & -1 & -1 \\ 0 & 0 & 1 & 0 & 0 & -1 & 0 & 1 & 1 & -1 & 1 & -1 & -1 & 1 & -1 \\ 0 & 0 & 0 & 1 & 0 & 0 & -1 & 1 & 1 & 1 & -1 & -1 & -1 & -1 & 1 \end{bmatrix} c$$
$$\omega_i = \begin{cases} 2/9, & i = 0 \\ 1/9, & i = 1, ..., 6, \\ 1/72, & i = 7, ..., 14 \end{cases} \quad c_s = c/\sqrt{3}, \quad (19d)$$

where $c \equiv \delta x/\delta t$ is the lattice speed with δx representing the lattice spacing.

It can be easily proved that the moments of the equilibrium phase-field distribution function satisfy

$$\sum_i f_i^{eq} = \phi; \quad \sum_i f_i^{eq}\mathbf{c}_i = (\phi\,\mathbf{u}+M\Theta\mathbf{n})/(1-\lambda); \quad \sum_i f_i^{eq}\mathbf{c}_i\mathbf{c}_i = \Gamma\phi/(1-\lambda)\mathbf{I}. \quad (20)$$

In order to determine $\mathbf{n}$ in the above equation using Eq. (11), the gradient term should be discretized first with suitable schemes. In the present study, the following second-order isotropic discretization [58–60] is adopted to calculate $\nabla\phi$,

$$\nabla\phi = \frac{1}{c_s^2\delta t}\sum_{i\neq 0}\omega_i\mathbf{c}_i\phi(\mathbf{x}+\mathbf{c}_i\delta t), \quad (21)$$

where ω_i, $\mathbf{c}_i$, and c_s are given by Eq. (19b) for 2D problems and (19d) for 3D problems. To avoid division by zero in the calculation of interface normal in Eq. (11), a small number $\varepsilon_0 = 10^{-12}$ is added to the denominator so that $\mathbf{n} = \nabla\phi/(|\nabla\phi|+\varepsilon_0)$.

The order parameter ϕ can be updated by taking the zeroth moment of the distribution function f_i after the streaming step.

$$\phi = \sum_i f_i. \quad (22)$$

Chapman-Enskog analysis (see Appendix A) demonstrates that the proposed model can recover the A-C equation (13) with an accuracy of $O(\delta t^2)$. With the similar Chapman-Enskog analysis, the model of Geier *et al.* [46,61] recovers the equation below (see Appendix B):

$$\frac{\partial\phi}{\partial t} + \nabla\cdot(\phi\,\mathbf{u}) = \nabla\cdot[M(\nabla\phi - \Theta\mathbf{n})]$$
$$+ M\{\partial_t\nabla\cdot(\phi\,\mathbf{u}+M\Theta\mathbf{n})$$
$$+ \nabla\cdot[\nabla\cdot(\phi\,\mathbf{uu})]\}/c_s^2 + O(\delta t^2). \quad (23)$$

As compared to the A-C equation (13), some additional terms, i.e., $M\{\partial_t\nabla\cdot(\phi\,\mathbf{u}+M\Theta\mathbf{n}) + \nabla\cdot[\nabla\cdot(\phi\,\mathbf{uu})]\}/c_s^2$, exist. Note from Eq. (19) that c_s is the sound speed that scales as $\bar{c}_s\delta x/\delta t$, where $\bar{c}_s$ is a pure number. The mobility M and velocity $\mathbf{u}$ are assumed to be determined by the physical problem. As such, they are independent of the chosen time and space discretization δx and δt. Thus, the additional terms are proportional to $(\delta t/\delta x)^2$ [62]. If taking the limits of $\delta x \to 0$ and $\delta t \to 0$ with $(\delta x)^2/\delta t$ constant, the error is $O(\delta t)$, .i.e., the accuracy of the scheme is of the first order. But, if taking $\delta x \to 0$ and $\delta t \to 0$ with $\delta x/\delta t$ constant, the scheme is only zeroth-order accurate [62]. If the equilibrium distribution function for ϕ is represented as a linear function of velocity $\mathbf{u}$, the additional term $\nabla\cdot[\nabla\cdot(\phi\,\mathbf{uu})]$ can be avoided [62]. Moreover, simple D2Q5 and D3Q7 lattice models can be used for two-dimensional and three-dimensional problems. In order to avoid another term $\partial_t\nabla\cdot(\phi\,\mathbf{u})$, Wang *et al.* [9] introduce a $\partial_t(\phi\,\mathbf{u})$ term (approximated by the first-order Eulerian scheme) in the source term of the LB equation. Moreover, in their Chapman-Enskog analysis, the $\partial_t\nabla\cdot(M\Theta\mathbf{n})$ term was neglected based on the assumption that $\mathbf{n}$ is of $O(\varepsilon)$, where ε is a small expansion parameter. However, in our opinion, $\mathbf{n}$ should be of $O(\varepsilon)$ because $\mathbf{n} = \nabla\phi/|\nabla\phi| = \varepsilon\nabla_1\phi/|\varepsilon\nabla_1\phi|$ and therefore the $\partial_t\nabla\cdot(M\Theta\mathbf{n})$ term could not be avoid by the model of Wang *et al.* [9] (see Appendixes A and B).

III. INTERFACE-CAPTURING TESTS

In this section, we test the performance of the proposed interface-capturing LB model using a series of benchmark cases including the diagonal translation of a circular interface, the rigid body rotation of a Zalesak disk, a 2D circular interface, and a 3D spherical interface in shear flows. The velocity fields are specified in advance; hence, only the phase fields need to be solved.

The numerical results obtained by the present model will be compared with those of the other two LB models for the conservative A-C equation: single-relaxation-time (SRT) model by Geier *et al.* [46,61] (denoted as model A) and SRT model by Wang *et al.* [9] (denoted as model B).

Unless otherwise stated, we adopt the D2Q5 and D3Q7 lattice models for 2D and 3D interfaces, respectively. The dimensionless parameters, Peclet number, Cahn number, and Courant-Friedrichs-Lewy (CFL) number are defined as

$$\text{Pe} = U_0 L_0/M, \quad \text{Ch} = W/L_0, \quad \text{CFL} = U_0\delta x/\delta t, \quad (24)$$

where U_0 and L_0 are the reference velocity and reference length, respectively. To quantitatively evaluate the accuracy of the present model and compare with the existing LB models, we introduce the L_2-norm relative error of the order parameter between numerical and analytical results as [46,48]

$$E_\phi = \sqrt{\frac{\sum_{\mathbf{x}}[\phi(\mathbf{x},t)-\phi(\mathbf{x},0)]^2}{\sum_{\mathbf{x}}\phi^2(\mathbf{x},0)}}, \quad (25)$$

where $\phi(\mathbf{x},0)$ is the initial distribution of the phase field at $t = 0$.

A. Diagonal translation of a circular interface

First we use the proposed model to simulate the motion of a 2D circular interface in a uniform velocity field $\mathbf{u} = (U_0, U_0)$ [9,14,46,48]. Initially, a circular interface with radius $R = L_0/5$ is located in the middle of a periodic $L_0 \times L_0$ computational domain with $L_0 = 200$. The distribution of the order parameter is initialized by

$$\phi(\mathbf{x}) = \frac{\phi_A+\phi_B}{2} + \frac{\phi_A-\phi_B}{2}\tanh\left(2\frac{R-|\mathbf{x}-\mathbf{x}_0|}{W}\right), \quad (26)$$

where $\mathbf{x}_0$ is the coordinate of the circle center. In the simulation, the CFL number and Cahn number are kept at 0.02 and 0.015, respectively, while the Peclet number varies from 125 to 8000. Theoretically, the interface would return to its initial location after a period $T = L_0/U_0$. The initial shape of the interface and the shapes after $10T$ obtained by different numerical models are compared in Fig. 1 and Fig. 2 for $\text{Pe} = 500$ and $\text{Pe} = 8000$, respectively. It can be found from Fig. 1 that, for $\text{Pe} = 500$, the present model, model A and model B can all obtain stable interface after 10 time cycles. However, for a larger Peclet number of $\text{Pe} = 8000$, as shown in Fig. 2, the interfaces obtained by both model A and model B
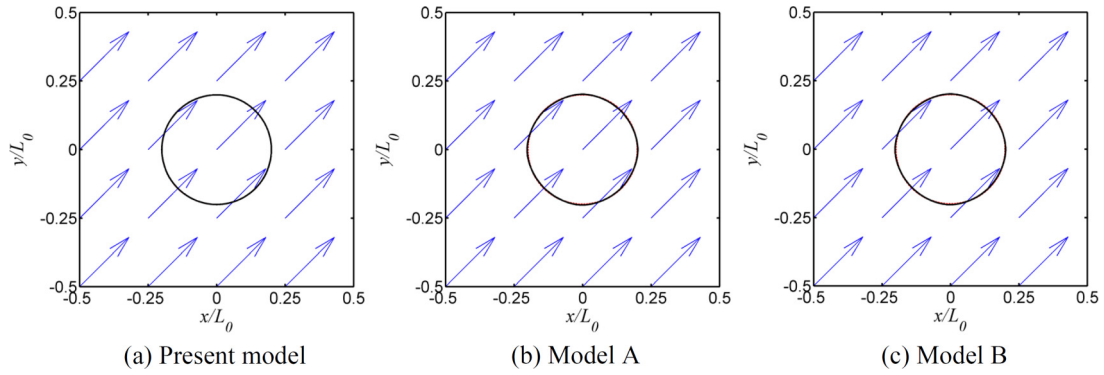
(a) Present model   (b) Model A   (c) Model B

FIG. 1. The circular interface translated diagonally at $t = 0$ (dashed line) and $t = 10\,\mathrm{T}$ (solid line) for CFL = 0.02, Pe = 500, and Ch = 0.015.

are twisted obviously due to the numerical instability. In contrast, the present method can still capture the interface shape stably. It is known that the Peclet number represents the rate of the fluid convection to diffusion, and determines the relative contribution of the above two mechanisms to the interface motion. Therefore, with the raise of Peclet number, numerical solution could become increasingly unstable due to the strong convection. To give a quantitative comparison of different models in accuracy when the numerical results are stable, the relative errors of three models are calculated and shown in Table I. From this table, it can be found that the present model produces more satisfactory results, while the relative errors of model A and model B almost identical for this particular case and are both relatively larger as compared with the present model.

B. Zalesak disk rotation

We then consider the rotational motion of a Zalesak disk [8,9,14,42,46,48,63]. As illustrated in Fig. 3, a slotted circular disk is initially located at the center of a periodic computational domain with $L_0 \times L_0$ lattice sites where $L_0 = 200$. The radius of the disk and the width of the slot are set as 80 and 15 lattice units, respectively. The rotation of the disk is driven by a velocity field of $u_x = -U_0 \pi y / L_0$, $u_y = U_0 \pi x / L_0$. Theoretically, the disk should return to its initial shape and location after one period $T = 2L_0 / U_0$. CFL number and Cahn

number are kept at 0.02 and 0.01, respectively, in the present test. Four values of mobility of 0.05, 0.01, 0.005, and 0.001 are considered so that the corresponding Peclet number are 80, 400, 800, and 4000, respectively. The evolutions with time of the interface shapes for Pe = 400 and Pe = 4000 are presented in Fig. 4 and Fig. 5, respectively. It can be found that the current method can track the interface accurately. Both model A and model B produce very similar results; therefore, the interfaces obtained by these two models are not plotted here. To quantitatively evaluate the performance of different models in the interface tracking, the relative errors of present results are compared with model A and model B as shown in Table II. The relative errors for model A and model B are almost identical for the case examined here, while the present model gives relatively lower errors, especially at the large Peclet numbers.

C. Circular interface in a smoothed shear flow

Neither of the above two cases deal with large topological change since the interface shapes remain unchanged during the evolution process. In order to check the capability of the present model in capturing interface deformation, we consider another test about the deformation of circular interface in a smoothed shear flow, which is regarded as one of the most stringent benchmarking problems as the interface undergoes a severe deformation [9,12,14,46]. Initially, a circular interface
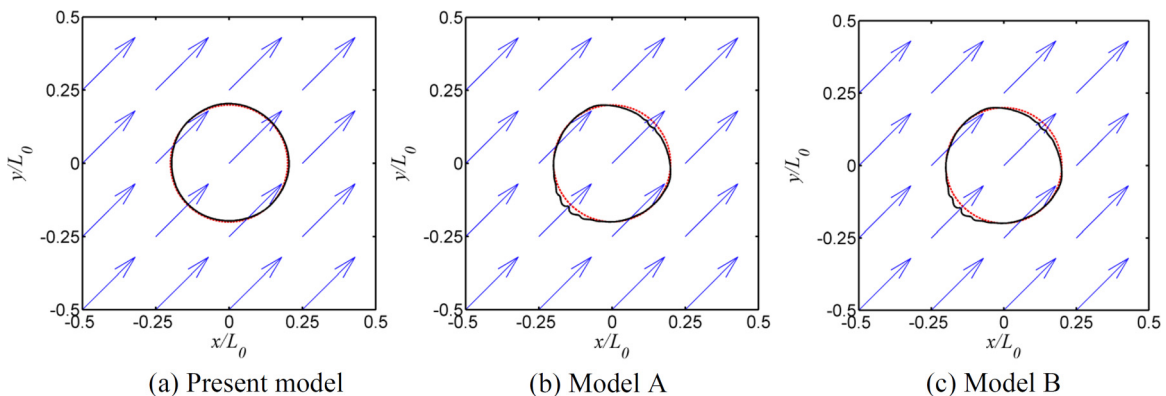

(a) Present model   (b) Model A   (c) Model B

FIG. 2. The circular interface translated diagonally at $t = 0$ (dashed line) and $t = 10\,\mathrm{T}$ (solid line) for CFL = 0.02, Pe = 8000, and Ch = 0.015.

TABLE I. Relative error for diagonal translation of a circular interface at $t = 10\,T$ for CFL $= 0.02$ and Ch $= 0.015$.

Model	Pe		
	125	500	2000
Present	0.0032	0.0021	0.0084
Model A	0.0363	0.0107	0.0600
Model B	0.0359	0.0106	0.0596

with radius $R = L_0/5$ is placed in the middle of a periodic $[0, L_0] \times [0, L_0]$ computational domain where $L_0 = 512$. The distribution of the order parameter is initialized by Eq. (26). The velocity field is time dependent and strongly nonlinear:

$$u_x(x, y, t) = -U_0 \sin(4\pi x/L_0) \sin(4\pi y/L_0) \cos(\pi t/T),$$
$$\text{(27a)}$$

$$u_y(x, y, t) = -U_0 \cos(4\pi x/L_0) \cos(4\pi y/L_0) \cos(\pi t/T),$$
$$\text{(27b)}$$

where U_0 is the reference velocity, $T = L_0/U_0$ is period. For CFL $= 0.02$, Pe $= 10\,240$ and Ch $= 1/256$, the topological changes of the interface during one period T can be found in Fig. 6. As seen from the figure, the interface undergoes transfiguration in the first half period and then reconstruction in the next half period. The largest topological change of the interface takes place at $t = T/2$, when thin filamentary structures are formed. After one period, the interface retunes to its original location with a relative error of 0.0125. For the same case, the relative errors of model A and model B are 0.0136 and 0.0139, respectively.

D. 3D spherical interface in a shear flow

In this section, we consider a 3D problem, a spherical interface in a shear flow [48,61,64]. Initially, a spherical interface with radius $R = L_0/5$ is located at $(3L_0/10, 3L_0/10, L_0/2)$ in a periodic domain of $[0, L_0] \times [0, L_0] \times [0, L_0]$ with $L_0 = 100$. The distribution of the order parameter is initialized by
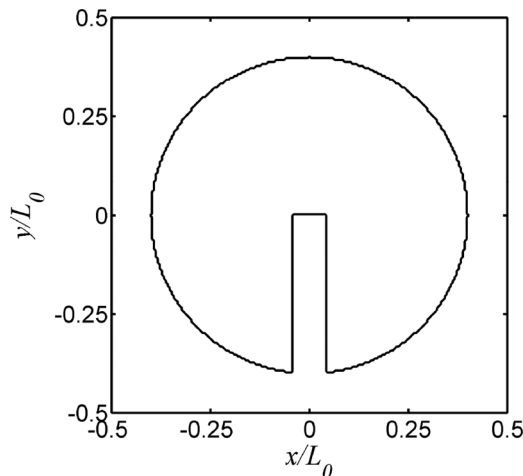

FIG. 3. Initial shape of the Zalesak disk.

Eq. (26), in which $\mathbf{x}_0$ stands for the coordinate of the sphere center here. The velocity field is given by

$$u_x = U_0\pi \cos(\pi x/L_0 - \pi/2)[\sin(\pi z/L_0 - \pi/2)$$
$$- \sin(\pi y/L_0 - \pi/2)]\cos(\pi t/T), \quad \text{(28a)}$$

$$u_y = U_0\pi \cos(\pi y/L_0 - \pi/2)[\sin(\pi x/L_0 - \pi/2)$$
$$- \sin(\pi z/L_0 - \pi/2)]\cos(\pi t/T), \quad \text{(28b)}$$

$$u_y = U_0\pi \cos(\pi z/L_0 - \pi/2)[\sin(\pi y/L_0 - \pi/2)$$
$$- \sin(\pi x/L_0 - \pi/2)]\cos(\pi t/T), \quad \text{(28c)}$$

where the period $T = 2L_0/U_0$. Theoretically, for this velocity field, flow direction will be reversed after $t = T/2$ so that the interface will return to its original position at $t = T$. (See the evolution of the interface shape for CFL $= 0.02$, Pe $= 200$, and Ch $= 0.03$ shown in Fig. 8.) The clear topology of the interface can be captured successfully, even at the thin tails. Although the original spherical shape cannot be fully recovered after one period, as shown in Fig. 7(h), the error is relatively small. The relative error of the order parameter after one period equals 0.0253.

IV. BINARY FLOW TESTS

In this section, the proposed model is used to capture the interface in the immiscible binary flow. The velocity fields are calculated with the model of Zu and He [42], in which D2Q9 and D3Q15 models are used for hydrodynamic properties in 2D and 3D, respectively. In the LB model of Zu and He [42], the following hydrodynamic equations for incompressible multiphase flows are recovered:

$$\nabla \cdot \mathbf{u} = 0, \quad \text{(29a)}$$

$$\rho \frac{\partial \mathbf{u}}{\partial t} + \rho \nabla \cdot (\mathbf{u}\mathbf{u}) = -\nabla p + \nabla \cdot [\mu(\nabla \mathbf{u} + \mathbf{u}\nabla)] + \mathbf{F}_s + \mathbf{F}_b,$$
$$\text{(29b)}$$

where p is the hydrodynamic pressure; $\mathbf{F}_b$ is the body force; $\mathbf{F}_s$ denotes the surface tension which is evaluated in a potential form as $\mathbf{F}_s = -\phi \nabla \mu_\phi$; ρ and μ are the density and dynamic viscosity, respectively. Let ρ_A and ρ_B be the densities in the bulk of fluids A and B, respectively; then ρ and μ can be calculated on the basis of phase-field variable ϕ as [42]

$$\rho = \frac{\phi - \phi_B}{\phi_A - \phi_B}(\rho_A - \rho_B) + \rho_B \quad \text{(30a)}$$

$$\mu = \frac{\mu_A\mu_B(\phi_A - \phi_B)}{(\phi - \phi_B)\mu_B + (\phi_A - \phi)\mu_A}. \quad \text{(30b)}$$

A. Stationary droplet

The stationary droplet is a widely used test for verifying multiphase models, especially for the evaluation of the spurious currents [38,53,55,59]. Here, we simulate this problem with the proposed model. Initially, a 2D circular droplet with radius $R = L_0/4$ is located at the center of a periodic $[-L_0/2, L_0/2] \times [-L_0/2, L_0/2]$ computational domain with $L_0 = 100$. The interface thickness is set as $W = 5$. The

(a) t=T/4; (b) t=T/2; (c) t=3T/4; (d) t=T
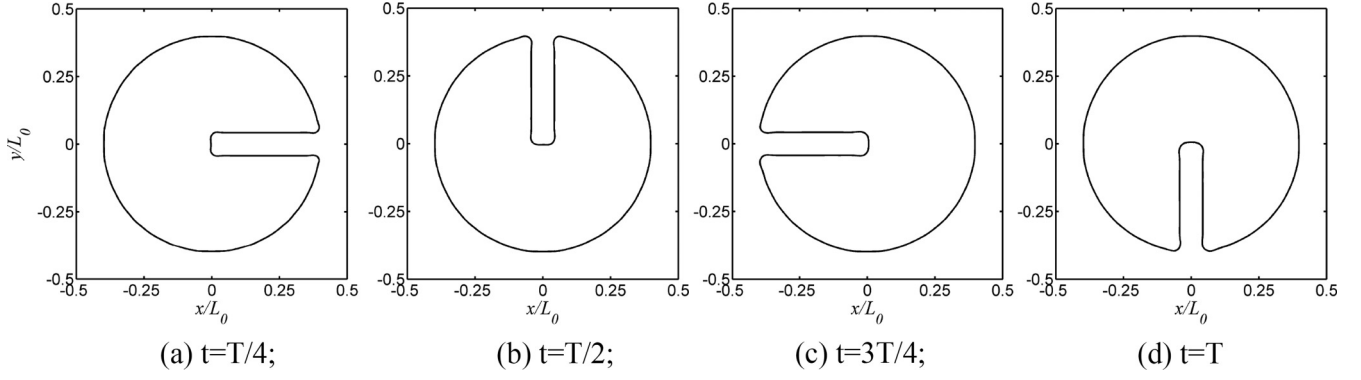
FIG. 4. Evolution of the interface shape at Pe = 400, Ch = 0.01.

distribution of the order parameter is initialized as

$$\phi(\mathbf{x}) = \frac{\phi_A + \phi_B}{2} + \frac{\phi_A - \phi_B}{2} \tanh\left(2\frac{R - |\mathbf{x} - \mathbf{x}_0|}{W}\right), \quad (31a)$$

where $\mathbf{x}_0$ is the coordinate of the droplet center. According to Eq. (30a), the initial density distribution can be given as

$$\rho(\mathbf{x}) = \frac{\rho_A + \rho_B}{2} + \frac{\rho_A - \rho_B}{2} \tanh\left(2\frac{R - |\mathbf{x} - \mathbf{x}_0|}{W}\right). \quad (31b)$$

The density ratio and viscosity ratio are set as $\rho_A/\rho_B = 1000$ and $\mu_A/\mu_B = 50$, respectively. The other parameters are given as $\phi_A = 1$, $\phi_B = -1$, $M = 0.001$.

Incompressible phase-field models usually suffer from the presence of the spurious currents at the fluid-fluid interface, especially when the densities of the fluids are unequal [65]. Generally, these spurious currents can be systematically suppressed by using the potential form of the surface tension and suitable discrete schemes [66]. To check the effects of the surface tension on the spurious currents, four values, $\sigma = 10^{-2}$, 10^{-3}, 10^{-4}, and 10^{-5}, are used for the tests. After 10^6 iterations, Figs. 8(a) and 8(b) show the interface locations and velocity fields for $\sigma = 10^{-2}$ and 10^{-5}, respectively. The solid lines represent the interface locations, the arrowed lines show the streamlines, and the background of the figures is colorized with the velocity magnitude $|\mathbf{u}|$. It can be seen from the figures that, due to the interfacial force applied, unphysical velocities occur in the flow fields and form vortices around the interfaces. The velocities in the direction normal to the

interface are rather small so that the spurious currents across the interface are suppressed effectively.

For the different values of the surface tensions, Table III presents the maximum velocity magnitudes $|\mathbf{u}|_{\max}$ and the relative errors of the densities $E_\rho = \sqrt{\sum_{\mathbf{x}} [\rho(\mathbf{x}, t) - \rho(\mathbf{x}, 0)]^2 / \sum_{\mathbf{x}} \rho^2(\mathbf{x}, 0)}$ at $t = 10^6 \, \delta t$, where $\rho(\mathbf{x}, 0)$ is given by Eq. (31b). Obviously, the spurious velocities increase with the surface tension. But, the values of E_ρ are always very small and basically independent of the change of the surface tension, which indicates that the interfacial currents are limited to a rather small quantity so that the local and global mass can be well conserved.

B. Spinodal decomposition

The spinodal decomposition [14,49,67–70] is a process of unmixing, i.e., phase separation, which usually takes place when imposing a small perturbation on the emulsifiers of two immiscible fluids. Here, in order to test the proposed model in dealing with phase separation, a 2D spinodal decomposition process is simulated using the model. In the simulation, a periodic computational domain of $L_0 \times L_0 = 150 \times 150$ is adopted. The order parameter is initialized with a small (1%) random perturbation,

$$\phi(\mathbf{x}) = \frac{\phi_A + \phi_B}{2} + (\phi_A - \phi_B)\left[\text{rand}(\mathbf{x}) - \frac{1}{6}\right], \quad (32)$$

where $\text{rand}(\mathbf{x})$ is a random function with the maximum amplitude of 0.01. The other parameters are given as $\rho_A = 10$,
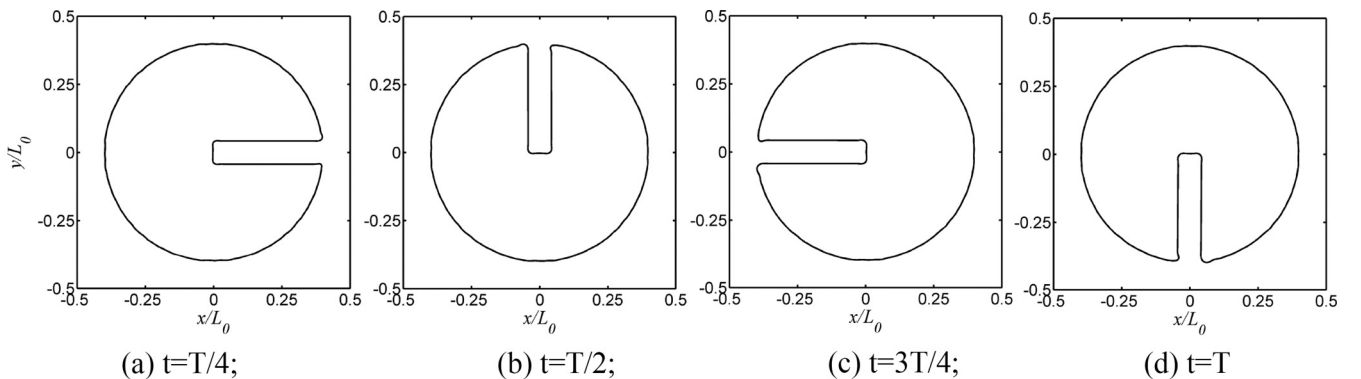

(a) t=T/4; (b) t=T/2; (c) t=3T/4; (d) t=T

FIG. 5. Evolution of the interface shape at Pe = 4000, Ch = 0.01.

TABLE II. Relative error for the rotating Zalesak disk at $t = \mathrm{T}$ for CFL $= 0.02$ and Ch $= 0.01$.

Model	Pe			
	80	400	800	4000
Present model	0.1226	0.1186	0.1170	0.1194
Model A	0.1307	0.1224	0.1209	0.1472
Model B	0.1307	0.1224	0.1209	0.1471

$\rho_B = 0.5$, $\mu_A = 5/3$, and $\mu_B = 1/12$, where ρ_A and ρ_B are the density of fluids A and B; μ_A and μ_B are the dynamic viscosity of fluids A and B, respectively. The reference time and velocity are defined as $T_0 = \mu_A L_0/\sigma$ and $U_0 = \sigma/\mu_A$, respectively. Figure 9 shows the phase distribution at various dimensionless time $t* = t/T_0$ for CFL $= 0.012$, Pe $= 180$, and Ch $= 4/150$, where the phase separation process can be observed. At the early stage, small fluctuations in density evolve into large-scale heterogeneities and the interfaces begin to separate different phases. Then, some tiny droplets with irregular shapes are formed in the system. These droplets coalesce with some of the others and grow in size, which eventually leads to the phase separation, as expected.

C. Rayleigh-Taylor instability

The Rayleigh-Taylor instability is a type of flow instability that takes place when a heavier fluid A rests on top of a lighter fluid B with an initial perturbation at the interface. This benchmark has been extensively investigated by many numerical approaches [7,27,41,71–76].
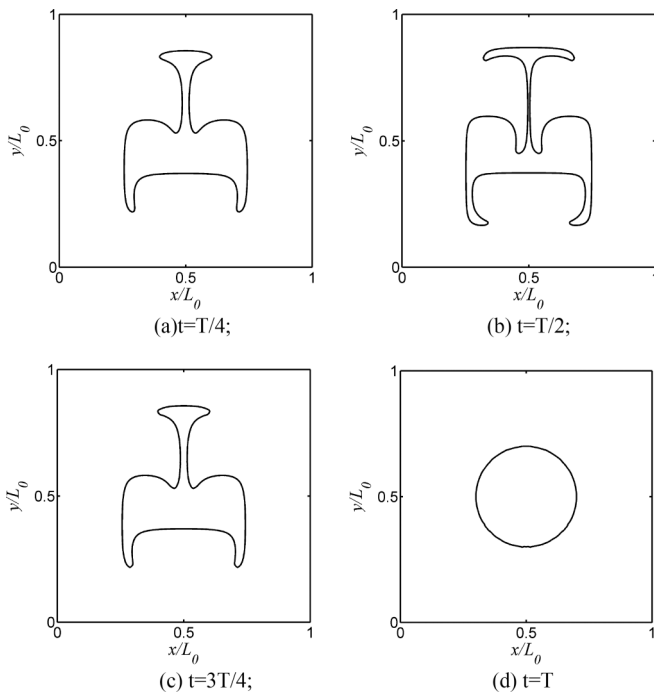

(a) t=T/4;

(b) t=T/2;

(c) t=3T/4;

(d) t=T

FIG. 6. Deformation of a circular interface in a smoothed shear flow at Pe $= 10\,240$, Ch $= 1/256$.

(a) t=0

(b) t=T/8

(c) t=T/4

(d) t=3T/8
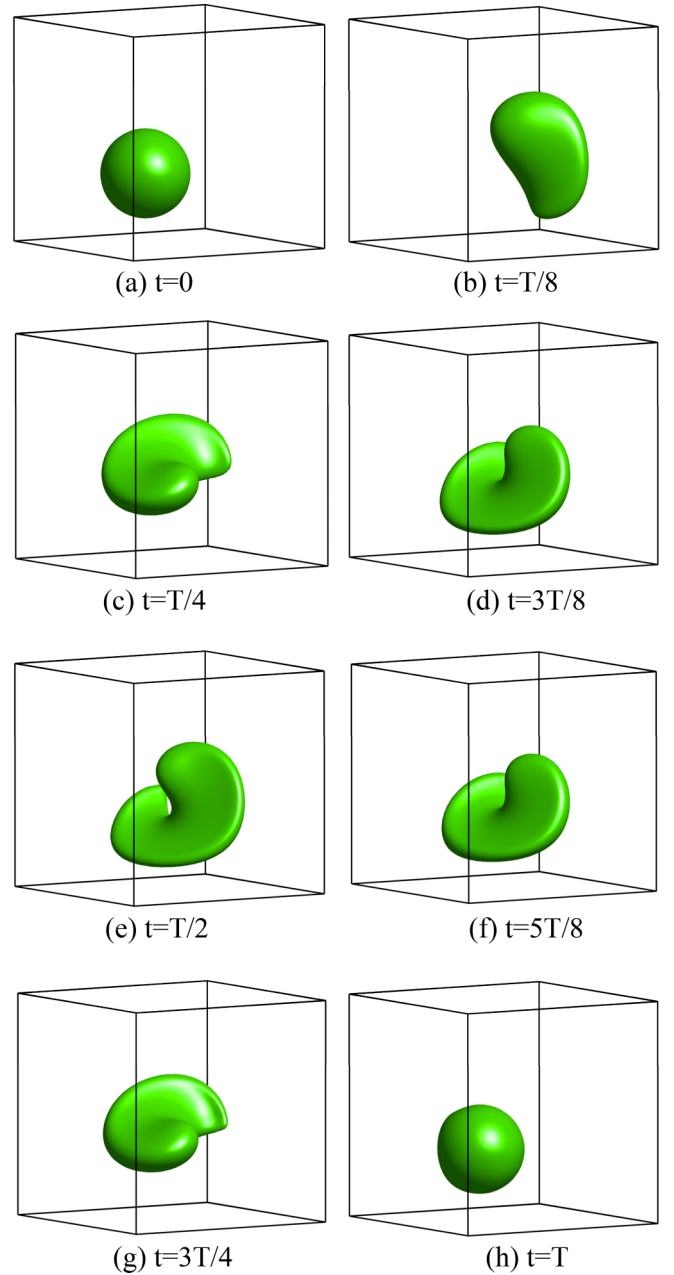
(e) t=T/2

(f) t=5T/8

(g) t=3T/4

(h) t=T

FIG. 7. Evolution of a spherical interface under shear flow for CFL $= 0.02$, Pe $= 200$, and Ch $= 0.03$.

We first consider a typical 2D Rayleigh-Taylor instability in a rectangular computational domain of $[-L_0/2, L_0/2] \times [-2L_0, 2L_0]$ with no-slip condition on the top and bottom walls and periodic boundary condition on the sides. Initially, two layers of the fluids at rest have an interface located at $y = 0.1L_0 \cos(2\pi x/L_0)$. In order to characterize the Rayleigh-Taylor instability problem, Atwood number $A_t = (\rho_A - \rho_B)/(\rho_A + \rho_B)$, Reynolds number $\mathrm{Re} = \rho_A L_0 U_0/\mu_A$, and capillary number $\mathrm{Ca} = \mu_A U_0/\sigma$ are introduced, where $U_0 = \sqrt{gL_0}$ is the reference velocity. To be consistent with the previous study [7,41,42,73,74], the dimensionless time $t* = t/\sqrt{L_0/gA_t}$ is introduced. A 200×800 grid is used for the simulation, i.e., $L_0 = 200$. The other parameters are set as $A_t = 0.5$, $\mathrm{Re} = 3000$, $\mathrm{Ca} = 100$, CFL $= 0.0707$, Pe $= 1000$,

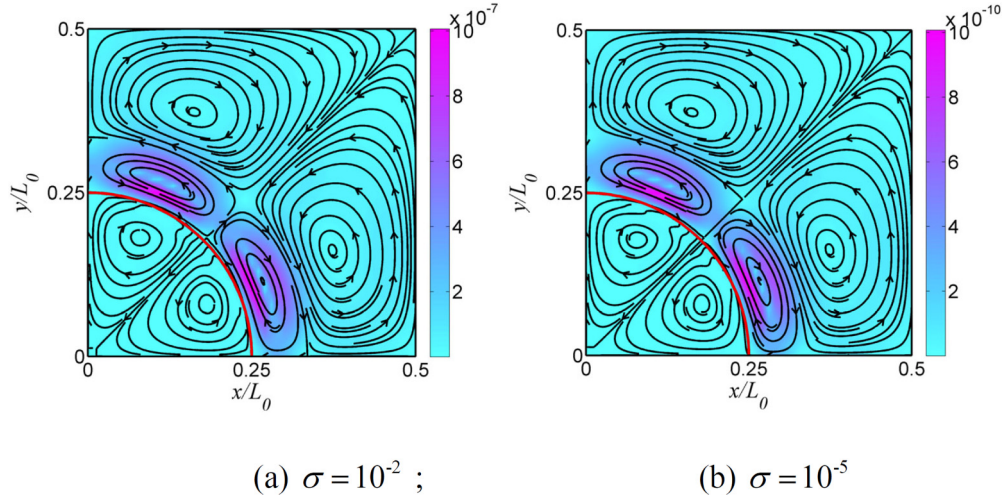(a) $\sigma = 10^{-2}$;   (b) $\sigma = 10^{-5}$

FIG. 8. Velocity field at $t = 10^6 \, \delta t$ (solid line: fluid-fluid interface; lines with arrow: streamlines; background color: velocity magnitude).

and Ch = 0.025. The viscosity ratio is $\mu_A/\mu_B = 1$. The time evolution of the interface for $t^* = 0 \sim 3.0$ is depicted in Fig. 10. It can be observed that the heavier fluid penetrates symmetrically into the lighter fluid to form a shape of "spike," with the generation of counter-rotating vortices. Meanwhile, the fingers of lighter fluid, named as "bubbles" here, are generated. The same flow regime can also be found in the work of Refs. [7,41,42,73,74]. Figure 11 shows the quantitative comparisons in the time evolution of dimensionless positions of the bubble and spike fronts. It is clear that the present results are in good agreement with the previously published data [7,41,42,73,74].

In order to demonstrate the accuracy and stability of the proposed model in dealing with a 3D binary fluid system, a simulation of a 3D Rayleigh-Taylor [27,42] is conducted. The computational domain for this case consists of a rectangular box of $[-L_0/2, L_0/2] \times [-L_0/2, L_0/2] \times [-2L_0, 2L_0]$. The interface between the two fluids is initially located at $z = 0.05L_0[\cos(2\pi x/L_0) + \cos(2\pi y/L_0)]$. The reference time and velocity are defined as $T_0 = \sqrt{L_0/g}$ and $U_0 = \sqrt{gL_0}$, respectively. The kinetic viscosity, ν, of the two fluids are set to be identical. The Reynolds number $\mathrm{Re} = U_0L_0/\nu$ and the Atwood number $A_t = (\rho_A - \rho_B)/(\rho_A + \rho_B)$ are set to be 128 and 0.5, respectively. A $64 \times 64 \times 256$ grid is used for the simulation, i.e., $L_0 = 64$. The other parameters are set as Ca = 960, CFL = 0.08, Pe = 1024, and Ch = 5/64. The evolution of the interface is shown in Fig. 12 at $t* = t/T_0 = 0 \sim 4.5$. Under the action of gravity, the heavy fluid falls to generate a spike and the light fluid rises to form a bubble. Meanwhile, four saddle points are formed at the middle of the four sides of the computational domain. The definitions of the points

tracked in the simulation can be observed in Fig. 12(c). Qualitatively, similar processes of interfacial deformation to those in Refs. [27,42] are obtained. A quantitative comparison is carried out by tracking the dimensionless positions of the spike, bubble, and saddle points. Figure 13 plots the current results and those reported in Ref. [27], which shows a close agreement. This indicates that the proposed model is able to simulate practical binary fluid systems with satisfying accuracy and stability.

V. CONCLUSIONS

In this study, we propose an LB model based on the conservative form A-C equation for phase field to track the interface of binary fluid systems. Chapman-Enskog analysis shows that the A-C equation can be correctly recovered by this model with second-order accuracy.

The model is benchmarked and validated against 2D and 3D interface tracking tests with known velocity fields and the binary flows problems, including the Zalesak disk rotation, the deformation of 2D circular interface and the 3D spherical interface in shear flows, the stationary droplet, the spinodal decomposition, and the 2D and 3D Rayleigh-Taylor instability. In the interface tracking tests, the currently proposed model shows better accuracy and stability than the previous models tested especially at higher Peclet numbers. In the binary flow tests, the present model is coupled with the model of Zu and He [42] for the velocity fields, and shows the satisfying performance in dealing with complicated situations.

It should be pointed out that in the present model, a $1 - \lambda$ term is introduced into the denominator of equilibrium distribution function, which may lead to large rounding error when τ_ϕ approaches 1.0, since $\lambda = 2\tau_\phi - 1$. However, the τ_ϕ that approaches 1.0 is absolutely unnecessary in the model. Therefore, in the simulation, such τ_ϕ should be avoided to eliminate the rounding error. A recommended range of τ_ϕ is from 0.6 to 0.9.

TABLE III. The maximum spurious velocities and the relative errors of the densities at different surface tensions.

	Surface tension σ			
	10^{-2}	10^{-3}	10^{-4}	10^{-5}
$|\mathbf{u}|_{\max}$	9.86×10^{-7}	1.01×10^{-7}	1.02×10^{-8}	1.02×10^{-9}
E_ρ	2.23×10^{-4}	2.19×10^{-4}	2.21×10^{-4}	2.23×10^{-4}
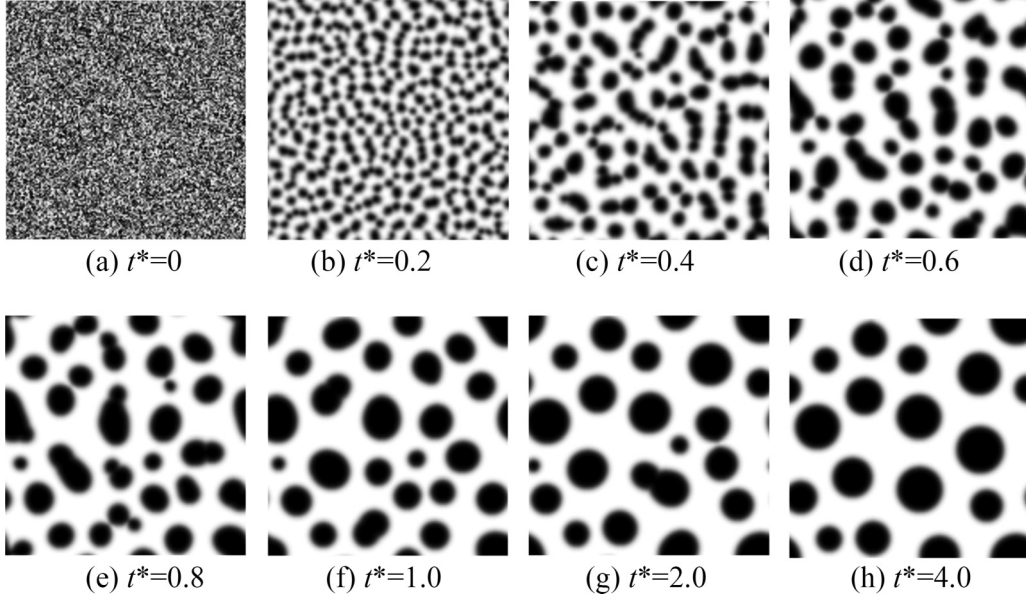
FIG. 9. Separation of binary fluid for CFL = 0.006, Pe = 180, and Ch = 4/150.

APPENDIX A: CHAPMAN-ENSKOG ANALYSIS OF THE PRESENT MODEL

In this appendix, a Chapman-Enskog analysis [77–79] is performed by introducing the following expansions of distribution function, time, and space derivatives:

$$f_i = f_i^{(0)}(\mathbf{x}, t) + \varepsilon f_i^{(1)}(\mathbf{x}, t) + \varepsilon^2 f_i^{(2)}(\mathbf{x}, t), \qquad (A1)$$

$$\partial_t = \varepsilon \partial_{t1} + \varepsilon^2 \partial_{t2}; \nabla = \varepsilon \nabla_1, \qquad (A2)$$

where ε is a small expansion parameter proportional to the ratio of the lattice spacing to a characteristic macroscopic length [77,78,80].

Taylor expansion of Eq. (15) gives

$$\left(\delta t D_i + \frac{\delta t^2}{2} D_i^2 \right) f_i = - \frac{f_i(\mathbf{x}, t) - f_i^{eq}(\mathbf{x}, t)}{\tau} + \lambda \left(\delta t \nabla_i + \frac{\delta t^2}{2} \nabla_i^2 \right) f_\alpha^{eq} + O(\delta t^3), \qquad (A3)$$
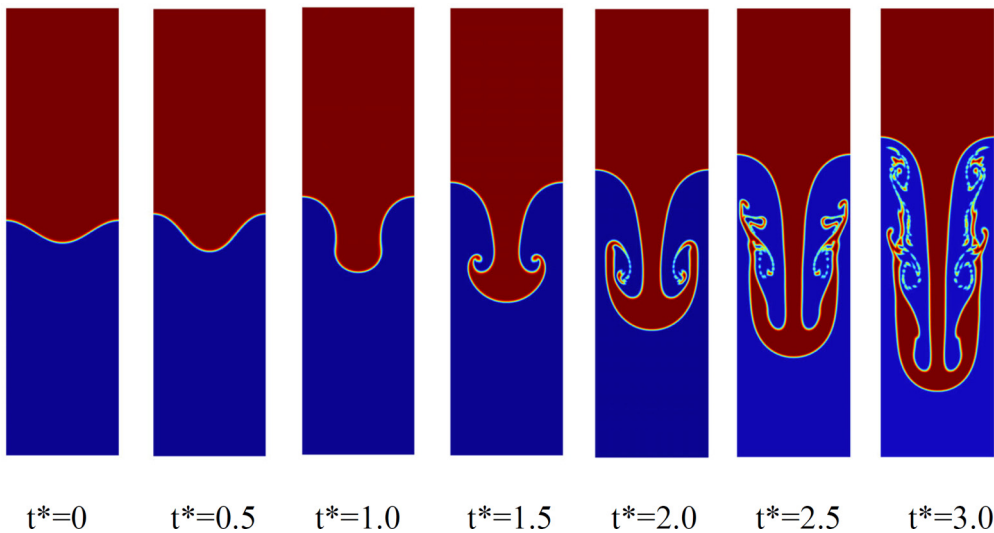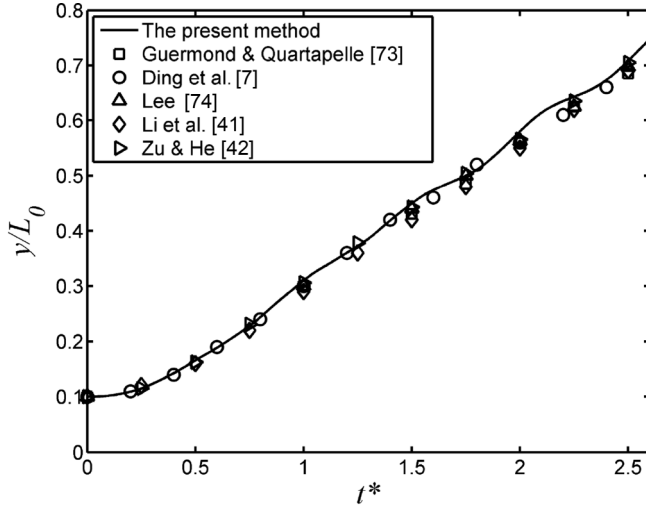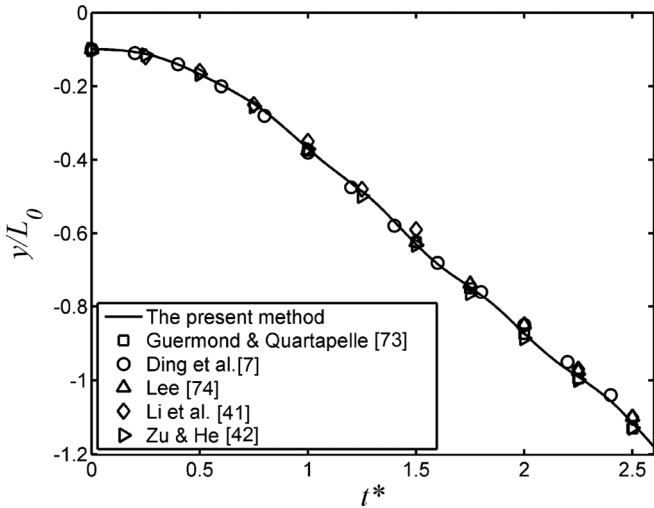

FIG. 10. Snapshots of the interface patterns of 2D Rayleigh-Taylor instability.

(a) bubble front

(b) spike front

FIG. 11. Time evolution of the bubble and spike fronts; comparative data are extracted from Refs. [7,41,42,73,74].

where $\boldsymbol{\nabla}_i = \mathbf{c}_i \cdot \boldsymbol{\nabla}$ and $D_i = \partial_t + \boldsymbol{\nabla}_i$. Substituting Eqs. (A1) and (A2) into Eq. (A3) and rearranging each item based on the power of ε, we have

$$O(\varepsilon^0): f_i^{(0)} = f_i^{eq} + O(\delta t^3), \tag{A4}$$

$$O(\varepsilon^1): \delta t(D_{1i} - \lambda \boldsymbol{\nabla}_{1i}) f_i^{(0)} = -f_i^{(1)}/\tau, \tag{A5}$$

$$O(\varepsilon^2): \delta t\left(\partial_{t2} f_i^{(0)} + D_{1i} f_i^{(1)}\right) + \frac{\delta t^2}{2}\left(D_{1i}^2 - \lambda \boldsymbol{\nabla}_{1i}^2\right) f_i^{(0)} = -f_i^{(2)}/\tau, \tag{A6}$$

where $\boldsymbol{\nabla}_{1i} = \mathbf{c}_i \cdot \boldsymbol{\nabla}_1$ and $D_{1i} = \partial_{t1} + \boldsymbol{\nabla}_{1i}$. Then, substitution of Eq. (A5) into Eq. (A6) gives

$$\delta t\, \partial_{t2} f_i^{(0)} - \tau \delta t^2 D_{1i}(D_{1i} - \lambda \boldsymbol{\nabla}_{1i}) f_i^{(0)} + \frac{\delta t^2}{2}\left(D_{1i}^2 - \lambda \boldsymbol{\nabla}_{1i}^2\right) f_i^{(0)}$$

$$= -f_\alpha^{(2)}/\tau. \tag{A7}$$

Note that, in the derivation of Eq. (A4), the interface normal $\mathbf{n}$ in f_α^{eq} [see Eq. (17)] has been regarded as $O(\varepsilon^0)$ because $\mathbf{n} = \boldsymbol{\nabla}\phi/|\boldsymbol{\nabla}\phi| = \varepsilon\boldsymbol{\nabla}_1\phi/|\varepsilon\boldsymbol{\nabla}_1\phi|$.

According to the expansions (A1), (A2), and (A4), Eq. (A5) $\times\varepsilon$ + Eq. (A7) $\times\varepsilon^2$ yields

$$[\partial_t + (1 - \lambda)\mathbf{c}_i \cdot \boldsymbol{\nabla}] f_i^{(0)}$$

$$= \delta t[(\tau - 1/2)\partial_t^2 + (2\tau - \tau\lambda - 1)\mathbf{c}_i \cdot \boldsymbol{\nabla}\partial_t$$

$$+ (1 - \lambda)(\tau - 1/2)\mathbf{c}_i\mathbf{c}_i\nabla^2] f_i^{(0)} - \frac{f_i - f_i^{eq}}{\tau\delta t} + O(\delta t^2). \tag{A8}$$

Combining with $\sum_i f_i = \sum_i f_i^{eq}$ given by Eqs. (20) and (22), summation of Eq. (A8) over i gives

$$\partial_t \sum_i f_i^{(0)} + (1 - \lambda)\boldsymbol{\nabla} \cdot \sum_i f_i^{(0)}\mathbf{c}_i$$

$$= \delta t\left[(\tau - 1/2)\partial_t^2 \sum_i f_i^{(0)} + (2\tau - \tau\lambda - 1)\partial_t\boldsymbol{\nabla}\right.$$

$$\cdot \sum_i f_i^{(0)}\mathbf{c}_i + (1 - \lambda)(\tau - 1/2)\boldsymbol{\nabla} \cdot \left(\boldsymbol{\nabla} \cdot \sum_i f_i^{(0)}\mathbf{c}_i\mathbf{c}_i\right)\right]$$

$$+ O(\delta t^2), \tag{A9}$$

which indicates

$$\partial_t \sum_i f_i^{(0)} + (1 - \lambda)\boldsymbol{\nabla} \cdot \sum_i f_i^{(0)}\mathbf{c}_i = O(\delta t). \tag{A10}$$

Therefore, Eq. (A9) can be rewritten as

$$\partial_t \sum_i f_i^{(0)} + (1 - \lambda)\boldsymbol{\nabla} \cdot \sum_i f_i^{(0)}\mathbf{c}_i$$

$$= \delta t\left[(\tau - \lambda/2 - 1/2)\partial_t\boldsymbol{\nabla} \cdot \sum_i f_i^{(0)}\mathbf{c}_i\right.$$

$$+ (1 - \lambda)(\tau - 1/2)\boldsymbol{\nabla} \cdot \left(\boldsymbol{\nabla} \cdot \sum_i f_i^{(0)}\mathbf{c}_i\mathbf{c}_i\right)\right] + O(\delta t^2). \tag{A11}$$

According to Eq. (16), the $(\tau - \lambda/2 - 1/2)\partial_t\boldsymbol{\nabla} \cdot \sum_i f_i^{(0)}\mathbf{c}_i$ term in Eq. (A11) equals zero. Then, substituting Eqs. (18) and (20) into Eq. (A11) leads to

$$\frac{\partial\phi}{\partial t} + \boldsymbol{\nabla} \cdot (\phi\,\mathbf{u}) = \boldsymbol{\nabla} \cdot [M(\boldsymbol{\nabla}\phi - \Theta\mathbf{n})] + O(\delta t^2). \tag{A12}$$

In other words, the conservative form Allen-Cahn equation (13) can be recovered by LB equation (15) with an accuracy of $O(\delta t^2)$.

(a) $t^* = 0$ (b) $t^* = 1$ (c) $t^* = 2$ (d) $t^* = 3$ (e) $t^* = 4$ (f) $t^* = 4.5$
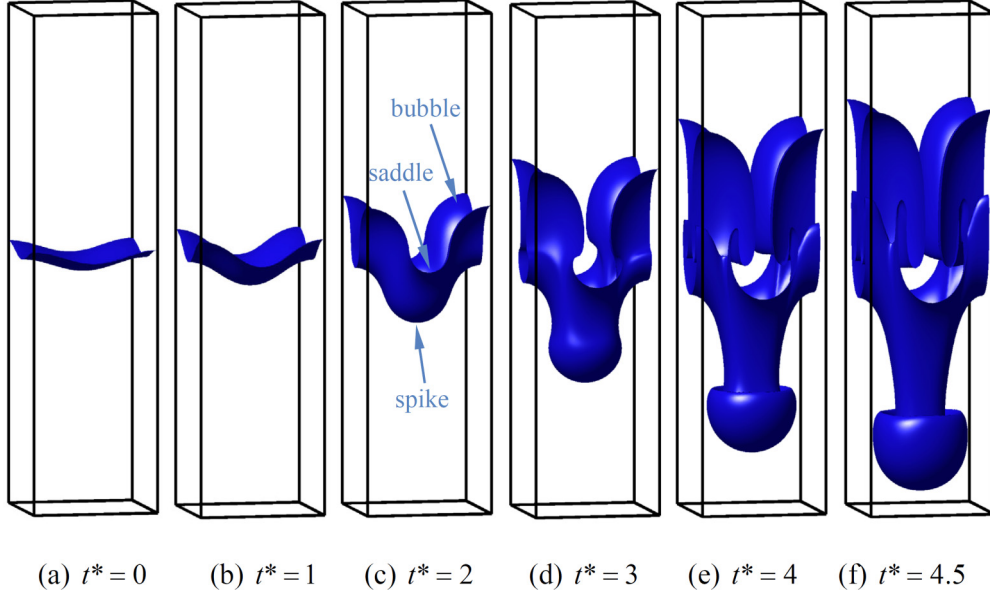
FIG. 12. Snapshots of 3D Rayleigh-Taylor instability

APPENDIX B: CHAPMAN-ENSKOG ANALYSIS OF GEIER'S MODEL

The LB equation of Geier's model [46] is written as

$$h_i(\mathbf{x} + \mathbf{c}_i \delta t, t + \delta t) - h_i(\mathbf{x}, t) = -\frac{h_i(\mathbf{x}, t) - h_i^{eq}(\mathbf{x}, t)}{\tau},$$
(B1)

where the equilibrium distribution function h_i^{eq} is given by

$$h_i^{eq} = \omega_i \phi \left[1 + \frac{\mathbf{c}_i \cdot \mathbf{u}}{c_s^2} + \frac{(\mathbf{c}_i \cdot \mathbf{u})^2}{2c_s^4} - \frac{\mathbf{u} \cdot \mathbf{u}}{2c_s^2} \right] + \omega_i \frac{M \Theta \mathbf{c}_i \cdot \mathbf{n}}{c_s^2}.$$
(B2)

It can be proved that the moments of the equilibrium distribution function satisfy

$$\sum_i h_i^{eq} = \phi; \quad \sum_i h_i^{eq} \mathbf{c}_i = (\phi \mathbf{u} + M \Theta \mathbf{n});$$
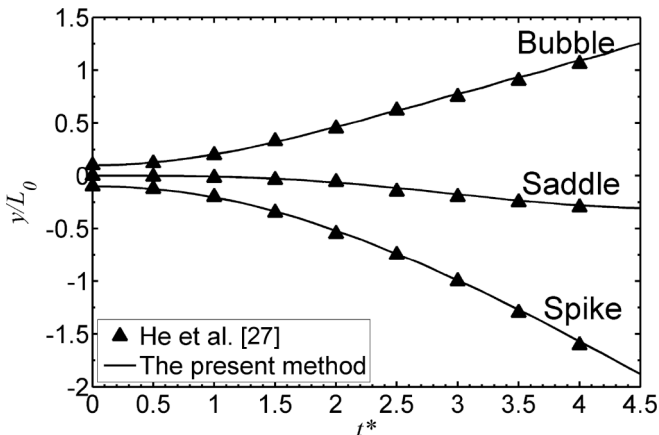

FIG. 13. Time evolution of the of bubble, saddle, and spike points.

$$\sum_i h_i^{eq} \mathbf{c}_i \mathbf{c}_i = \phi c_s^2 \mathbf{I} + \phi \mathbf{uu}$$
(B3)

A multiscaling analysis is carried out by introducing the following expansions:

$$h_i = h_i^{(0)}(\mathbf{x}, t) + \varepsilon h_i^{(1)}(\mathbf{x}, t) + \varepsilon^2 h_i^{(2)}(\mathbf{x}, t),$$
(B4)

$$\partial_t = \varepsilon \partial_{t1} + \varepsilon^2 \partial_{t2}; \mathbf{\nabla} = \varepsilon \mathbf{\nabla}_1.$$
(B5)

Taylor expansion of Eq. (B1) yields

$$\left(\delta t D_i + \frac{\delta t^2}{2} D_i^2 \right) h_i = -\frac{h_i(\mathbf{x}, t) - h_i^{eq}(\mathbf{x}, t)}{\tau},$$
(B6)

where $D_i = \partial_t + \mathbf{c}_i \cdot \mathbf{\nabla}$. Substituting Eqs. (B4) and (B5) into Eq. (B6) and treating the terms in the zeroth-, first-, and second order of ε separately, we have

$$O(\varepsilon^0) : h_i^{(0)} = h_i^{eq} + O(\delta t^3),$$
(B7)

$$O(\varepsilon^1) : \delta t D_{1i} h_i^{(0)} = -h_i^{(1)}/\tau,$$
(B8)

$$O(\varepsilon^2) : \delta t \left(\partial_{t2} h_i^{(0)} + D_{1i} h_i^{(1)} \right) + \frac{\delta t^2}{2} D_{1i}^2 h_i^{(0)} = -h_i^{(2)}/\tau,$$
(B9)

where $D_{1i} = \partial_{t1} + \mathbf{c}_i \cdot \mathbf{\nabla}_1$. Substitution of Eq. (B8) into Eq. (B9) gives

$$\delta t \partial_{t2} h_\alpha^{(0)} + (1/2 - \tau) \delta t^2 D_{1i}^2 h_i^{(0)} = -h_i^{(2)}/\tau.$$
(B10)

Using Eqs. (B4), (B5), and (B7), Eq. (B8) $\times \varepsilon$ + Eq. (B10) $\times \varepsilon^2$ yields

$$[\partial_t + \mathbf{c}_i \cdot \mathbf{\nabla}] h_i^{(0)} = -\frac{h_i - h_i^{eq}}{\tau \delta t}$$

$$+ \delta t (\tau - 1/2)(\partial_t + \mathbf{c}_i \cdot \nabla)^2 h_i^{(0)} + O(\delta t^2).$$
(B11)

Summation of Eq. (B11) over i and using $\sum_i h_i = \sum_i h_i^{eq} = \phi$ [46], one gets

$$\partial_t \sum_i h_i^{(0)} + \nabla \cdot \sum_i h_i^{(0)} \mathbf{c}_i$$

$$= \delta t (\tau - 1/2) \left[\partial_t^2 \sum_i h_i^{(0)} + 2 \partial_t \nabla \cdot \sum_i h_i^{(0)} \mathbf{c}_i \right.$$

$$\left. + \nabla \cdot \left(\nabla \cdot \sum_i h_i^{(0)} \mathbf{c}_i \mathbf{c}_i \right) \right] + O(\delta t^2), \quad \text{(B12)}$$

which indicates

$$\partial_t \sum_i h_i^{(0)} + \nabla \cdot \sum_i h_i^{(0)} \mathbf{c}_i = O(\delta t). \quad \text{(B13)}$$

Using Eq. (B13), the first term and a part of the second term in square brackets in Eq. (B12) can be neglected as $O(\delta t^2)$. Thus,

$$\partial_t \sum_i h_i^{(0)} + \nabla \cdot \sum_i h_i^{(0)} \mathbf{c}_i$$

$$= \delta t (\tau - 1/2) \left[\partial_t \nabla \cdot \sum_i h_i^{(0)} \mathbf{c}_i \right.$$

$$\left. + \nabla \cdot \left(\nabla \cdot \sum_i h_i^{(0)} \mathbf{c}_i \mathbf{c}_i \right) \right] + O(\delta t^2). \quad \text{(B14)}$$

Then, substituting Eqs. (B3) into Eq. (B14) gives

$$\frac{\partial \phi}{\partial t} + \nabla \cdot (\phi \mathbf{u} + M \Theta \mathbf{n})$$

$$= \delta t (\tau - 1/2) \{ \partial_t \nabla \cdot (\phi \mathbf{u} + M \Theta \mathbf{n})$$

$$+ \nabla \cdot [\nabla \cdot (\phi c_s^2 \mathbf{I} + \phi \mathbf{u} \mathbf{u})] \} + O(\delta t^2). \quad \text{(B15)}$$

Noting that $M = c_s^2 (\tau - 1/2) \delta t$ [46], Eq. (B15) can be rewritten as

$$\frac{\partial \phi}{\partial t} + \nabla \cdot (\phi \mathbf{u})$$

$$= \nabla \cdot [M(\nabla \phi - \Theta \mathbf{n})] + M \{ \partial_t \nabla \cdot (\phi \mathbf{u} + M \Theta \mathbf{n})$$

$$+ \nabla \cdot [\nabla \cdot (\phi \mathbf{u} \mathbf{u})] \} / c_s^2 + O(\delta t^2) \quad \text{(B16)}$$

which is the equation recovered by Geier's model.

[1] C. W. Hirt and B. D. Nichols, J. Comput. Phys. **39**, 201 (1981).

[2] M. Sussman, P. Smereka, and S. Osher, J. Comput. Phys. **114**, 146 (1994).

[3] G. Tryggvason, B. Bunner, A. Esmaeeli, D. Juric, N. Al-Rawahi, W. Tauber, J. Han, S. Nas, and Y. J. Jan, J. Comput. Phys. **169**, 708 (2001).

[4] D. M. Anderson, G. B. McFadden, and A. A. Wheeler, Annu. Rev. Fluid Mech. **30**, 139 (1998).

[5] D. Jacqmin, J. Comput. Phys. **155**, 96 (1999).

[6] V. E. Badalassi, H. D. Ceniceros, and S. Banerjee, J. Comput. Phys. **190**, 371 (2003).

[7] H. Ding, P. D. M. Spelt, and C. Shu, J. Comput. Phys. **226**, 2078 (2007).

[8] H. W. Zheng, C. Shu, and Y. T. Chew, Phys. Rev. E **72**, 056705 (2005).

[9] H. L. Wang, Z. H. Chai, B. C. Shi, and H. Liang, Phys. Rev. E **94**, 033304 (2016).

[10] M. R. Swift, E. Orlandini, W. R. Osborn, and J. M. Yeomans, Phys. Rev. E **54**, 5041 (1996).

[11] J. J. Huang, C. Shu, and Y. T. Chew, Int. J. Numer. Methods Fluids **60**, 203 (2009).

[12] H. Liang, B. C. Shi, Z. L. Guo, and Z. H. Chai, Phys. Rev. E **89**, 053320 (2014).

[13] Y. Li, X. D. Niu, Y. Wang, A. Khan, and Q. Z. Li, Int J Multiphase Flow **116**, 100 (2019).

[14] Z. R. Yang, C. W. Zhong, and C. S. Zhuo, Phys. Rev. E **99**, 043302 (2019).

[15] J. W. Cahn and J. E. Hilliard, J. Chem. Phys. **28**, 258 (1958).

[16] J. W. Cahn and J. E. Hilliard, J. Chem. Phys. **31**, 688 (1959).

[17] Y. Sun and C. Beckermann, J. Comput. Phys. **220**, 626 (2007).

[18] P. H. Chiu and Y. T. Lin, J. Comput. Phys. **230**, 185 (2011).

[19] P. T. Yue, C. F. Zhou, and J. J. Feng, J. Comput. Phys. **223**, 1 (2007).

[20] L. Zheng, T. Lee, Z. L. Guo, and D. Rumschitzki, Phys. Rev. E **89**, 033302 (2014).

[21] X. Zhao, B. Dong, and W. Z. Li, Int. J. Heat Mass Transfer **109**, 807 (2017).

[22] X. Zhao, B. Dong, W. Z. Li, and B. L. Dou, Appl. Therm. Eng. **111**, 1477 (2017).

[23] W. Gong, Y. Y. Yan, S. Chen, and E. Wright, Int. J. Heat Mass Transfer **125**, 323 (2018).

[24] A. Montessori, M. Lauricella, N. Tirelli, and S. Succi, J. Fluid Mech. **872**, 327 (2019).

[25] A. Montessori, M. Lauricella, A. Tiribocchi, and S. Succi, Phys. Rev. Fluids **4**, 072201 (2019).

[26] S. Chen and G. D. Doolen, Annu. Rev. Fluid Mech. **30**, 329 (1998).

[27] X. Y. He, R. Y. Zhang, S. Y. Chen, and G. D. Doolen, Phys. Fluids **11**, 1143 (1999).

[28] S. Succi, *The Lattice Boltzmann Equation for Fluid Dynamics and Beyond* (Clarendon Press, Oxford, 2001).

[29] C. K. Aidun and J. R. Clausen, Annu. Rev. Fluid Mech. **42**, 439 (2010).

[30] G. Falcucci, S. Ubertini, C. Biscarini, S. Di Francesco, D. Chiappini, S. Palpacelli, A. De Maio, and S. Succi, Commun. Comput. Phys. **9**, 269 (2011).

[31] S. Chen, Y. Y. Yan, and W. Gong, Int. J. Heat Mass Transfer **107**, 862 (2017).

[32] W. N. Zhou, Y. Y. Yan, X. L. Liu, and B. Q. Liu, Adv. Eng. Softw. **107**, 51 (2017).

[33] A. Xu, L. Shi, and T. S. Zhao, Int. J. Heat Mass Transfer **109**, 577 (2017).

[34] W. N. Zhou, Y. Y. Yan, X. L. Liu, H. X. Chen, and B. Q. Liu, Int. Commun. Heat Mass **97**, 39 (2018).

[35] Y. Y. Yan and Y. Q. Zu, J. Comput. Phys. **227**, 763 (2007).

[36] Y. Y. Yan and Y. Q. Zu, Int. J. Heat Mass Transfer **51**, 2519 (2008).

[37] Y. Q. Zu and Y. Y. Yan, Sci. Rep. **6**, 19281 (2016).

[38] H. W. Zheng, C. Shu, and Y. T. Chew, J. Comput. Phys. **218**, 353 (2006).

[39] J. S. Rowlinson and B. Widom, *Molecular Theory of Capillarity* (Clarendon, Oxford, 1989).

[40] D. Jacqmin, J. Fluid Mech. **402**, 57 (2000).

[41] Q. Li, K. H. Luo, Y. J. Gao, and Y. L. He, Phys. Rev. E **85**, 026704 (2012).

[42] Y. Q. Zu and S. He, Phys. Rev. E **87**, 043301 (2013).

[43] H. Liang, Z. H. Chai, B. C. Shi, Z. L. Guo, and T. Zhang, Phys. Rev. E **90**, 063311 (2014).

[44] H. Liang, B. C. Shi, and Z. H. Chai, Phys. Rev. E **93**, 013308 (2016).

[45] Y. Hu, Q. He, D. C. Li, Y. Li, and X. D. Niu, Comput. Fluids **193** 104291 (2019).

[46] M. Geier, A. Fakhari, and T. Lee, Phys. Rev. E **91**, 063309 (2015).

[47] A. Fakhari, M. Geier, and T. Lee, J. Comput. Phys. **315**, 434 (2016).

[48] F. Ren, B. W. Song, M. C. Sukop, and H. B. Hu, Phys. Rev. E **94**, 023311 (2016).

[49] H. Liang, J. R. Xu, J. X. Chen, H. L. Wang, Z. H. Chai, and B. C. Shi, Phys. Rev. E **97**, 033309 (2018).

[50] T. Mitchell, C. Leonardi, and A. Fakhari, Int. J. Multiphase Flow **107**, 1 (2018).

[51] A. Fakhari and D. Bolster, J. Comput. Phys. **334**, 620 (2017).

[52] J. Kim, J. Comput. Phys. **204**, 784 (2005).

[53] A. Begmohammadi, R. Haghani-Hassan-Abadi, A. Fakhari, and D. Bolster, Phys. Rev. E **102**, 023305 (2020).

[54] O. Penrose and P. C. Fife, Physica D **43**, 44 (1990).

[55] A. Fakhari and M. H. Rahimian, Phys. Rev. E **81**, 036707 (2010).

[56] A. J. Briant and J. M. Yeomans, Phys. Rev. E **69**, 031603 (2004).

[57] S. M. Allen and J. W. Cahn, Acta Metallurgica **24**, 425 (1976).

[58] T. Lee and C. L. Lin, J. Comput. Phys. **206**, 16 (2005).

[59] T. Lee and P. F. Fischer, Phys. Rev. E **74**, 046709 (2006).

[60] X. Shan, Phys. Rev. E **73**, 047701 (2006).

[61] A. Fakhari, M. Geier, and D. Bolster, Comput. Math. Appl. **78**, 1154 (2019).

[62] B. Chopard, J. L. Falcone, and J. Latt, Eur. Phys. J.-Spec. Top. **171**, 245 (2009).

[63] S. T. Zalesak, J. Comput. Phys. **31**, 335 (1979).

[64] H. W. Zheng, C. Shu, Y. T. Chew, and J. H. Sun, Int. J. Numer. Methods Fluids **56**, 1653 (2008).

[65] K. Yang and Z. L. Guo, Phys. Rev. E **93**, 043303 (2016).

[66] Q. Lou, Z. L. Guo, and B. C. Shi, Epl-Europhys Lett. **99**, 64005 (2012).

[67] X. W. Shan and H. D. Chen, Phys. Rev. E **47**, 1815 (1993).

[68] W. R. Osborn, E. Orlandini, M. R. Swift, J. M. Yeomans, and J. R. Banavar, Phys. Rev. Lett. **75**, 4031 (1995).

[69] J. Chin and P. V. Coveney, Phys. Rev. E **66**, 016303 (2002).

[70] A. G. Xu, G. Gonnella, and A. Lamura, Physica A **331**, 10 (2004).

[71] G. Tryggvason, J. Comput. Phys. **75**, 253 (1988).

[72] X. Y. He, S. Y. Chen, and R. Y. Zhang, J. Comput. Phys. **152**, 642 (1999).

[73] J. L. Guermond and L. Quartapelle, J. Comput. Phys. **165**, 167 (2000).

[74] L. Lee, Comput. Fluids **39**, 1022 (2010).

[75] D. Chiappini, G. Bella, S. Succi, F. Toschi, and S. Ubertini, Commun. Comput. Phys. **7**, 423 (2010).

[76] D. Chiappini, G. Bella, S. Succi, and S. Ubertini, Int. J. Mod. Phys. C **20**, 1803 (2009).

[77] J. M. Buick and C. A. Greated, Phys. Rev. E **61**, 5307 (2000).

[78] Z. L. Guo, C. G. Zheng, and B. C. Shi, Phys. Rev. E **65**, 046308 (2002).

[79] F. Liu, W. P. Shi, and F. F. Wu, Appl. Math. Comput. **274**, 331 (2016).

[80] Z. L. Guo, B. C. Shi, and N. C. Wang, J. Comput. Phys. **165**, 288 (2000).